Puffing ultrathin oxides with nonlayered structures

Kaisi Liu†, Hongrun Jin†, Liwei Huang†, Yongxin Luo, Zehao Zhu, Simin Dai, Xinyan Zhuang, Zidong Wang, Liang Huang*, Jun Zhou

Two-dimensional (2D) oxides have unique electrical, optical, magnetic, and catalytic properties, which are promising for a wide range of applications in different fields. However, it is difficult to fabricate most oxides as 2D materials unless they have a layered structure. Here, we present a facile strategy for the synthesis of ultrathin oxide nanosheets using a self-formed sacrificial template of carbon layers by taking advantage of the Maillard reaction and violent redox reaction between glucose and ammonium nitrate. To date, 36 large-area ultrathin oxides (with thickness ranging from ~1.5 to ~4 nm) have been fabricated using this method, including rare-earth oxides, transition metal oxides, III-main group oxides, II-main group oxides, complex perovskite oxides, and high-entropy oxides. In particular, the as-obtained perovskite oxides exhibit great electrocatalytic activity for oxygen evolution reaction in an alkaline solution. This facile, universal, and scalable strategy provides opportunities to study the properties and applications of atomically thin oxide nanomaterials.

INTRODUCTION

Two-dimensional (2D) oxides, consisting of thin crystalline layers at the atomic level, have aroused notable interest because of their fascinating properties for efficient energy storage and conversion technologies (1–8). However, ultrathin 2D oxide nanosheets tend to restack together into a thick plate-like structure, which markedly decreases active surface and prolongs ion transport pathways (9). The porous 2D oxides can effectively alleviate this issue by improving ion-accessible surface area and exposing abundant active sites (9–11), which are beneficial in various applications such as electrocatalysis (12, 13), alkali-ion batteries (10, 13, 14), and Li-O$_2$ batteries (15). Moreover, the porous 2D oxides with flexible valence can improve the electrocatalytic activity by generating many defective atoms (such as edge sites) in some case (12, 13). In general, the potential for practical application of 2D oxide materials mainly depends on the availability of a facile and scalable synthesis strategy. To date, various strategies have been developed for fabrication of 2D oxides, including vapor deposition methods and liquid-phase synthesis (wet-chemical synthesis and liquid exfoliation). Typically, vapor deposition methods include physical and chemical vapor deposition synthesis that favors to produce high-quality, large-area, and thickness-controllable oxide nanosheets, which is promising for studying their physical properties (16–21). However, this method usually involves complex and harsh synthesis processes, suffers from low yield, and is unsuitable for practical applications. In contrast, wet-chemical synthesis method is regarded as an efficient way to produce ultrathin 2D oxides due to its low cost, high yield, and simple operations (22–24). In most cases, however, this strategy requires surfactants or templates to facilitate the formation of 2D morphology that needs an extra tedious purification process. For the liquid exfoliation, ultrathin 2D materials can be fabricated mainly from the precursors with an intrinsically layered structure (25–27). Since most oxides have nonlayered structures, the formation of nanosheets via liquid phase exfoliation is difficult (28). Thus, it is highly desirable and significant to develop an efficient and universal strategy for large-scale synthesis of 2D oxides.

Glucose is a classical food raw material for desserts. In particular, molten glucose can be readily molded into different shapes because of its high viscosity. Inspired by the "black powder" of China, when the nitrate oxidizer is in contact with reducing agents of carbon and sulfur at high temperature, the mixture could instantly react to produce a large amount of gases, including NO$_x$, CO$_2$, and SO$_x$, leading to a rapid increase in volume (29, 30). It can be imagined that by heating a mixture of glucose and nitrate to high temperature, the produced gas could blow the molten glucose to form a layered structure. Here, we develop a self-templated strategy to synthesize many nonlayered porous oxide nanosheets without any further purification step by using the sacrificial layered carbon template, which is constructed by the Maillard reaction (31, 32) and violent redox reaction between ammonium nitrate and glucose. Unlike the gel-blowing strategy, which requires long time and complex procedures to prepare gel precursors (13), this method allows the preparation of various porous oxide nanosheets in a simple one-step process. In this work, we have successfully fabricated 36 ultrathin oxide nanosheets using this strategy, including rare-earth oxides, transition metal oxides, III-main group oxides, and unusual perovskite oxides, regardless of high synthesis temperature. The as-obtained LaFeO$_3$ (LFO) nanosheets demonstrated great oxygen evolution reaction (OER) performance with a low onset overpotential (~112.55 mV) and a small overpotential (~303.52 mV at 10 mA cm$^{-2}_{disk}$) in 1 M KOH solution.

RESULTS

Synthesis and characterizations of ultrathin porous oxide nanosheets

Figure 1A shows the schematic diagram for the preparation of oxides. In a typical synthesis protocol, ammonium nitrate, glucose, and metal salts are uniformly mixed in a mortar, followed by annealing in a muffle furnace to obtain oxide foam (33) that consists of ultrathin porous oxide nanosheets (movie S1). The optical photograph of the prepared oxide foam of Nd$_2$O$_3$, which is made of porous ultrathin nanosheets, is shown in Fig. 1B. The morphology of the two random areas of Nd$_2$O$_3$ material is confirmed to be flexible and curled nanosheets with lateral dimensions up to tens of micrometers by scanning electron microscopy (SEM) (Fig. 1, C and D), indicating the good uniformity of Nd$_2$O$_3$ nanosheets. According to the transmission

Wuhan National Laboratory for Optoelectronics, Huazhong University of Science and Technology, Wuhan 430074, China.
*Corresponding author. Email: huangliang421@hust.edu.cn
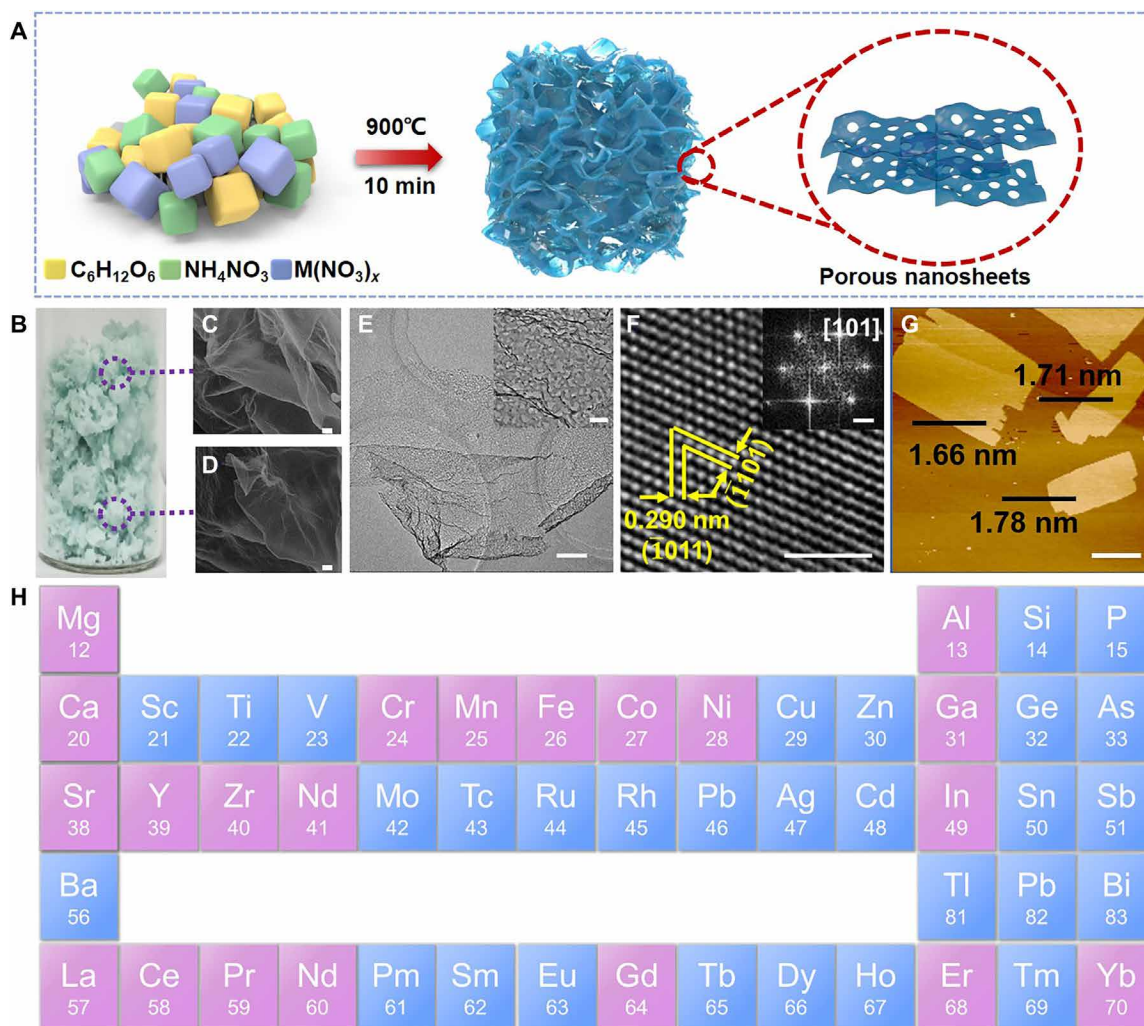†These authors contributed equally to this work.

Fig. 1. Preparation of nonlayered oxides. (**A**) Schematic diagram of the porous ultrathin oxide nanosheets prepared using the expansion method. (**B**) Optical photograph of the prepared porous ultrathin Nd_2O_3 nanosheets. (**C** and **D**) SEM images of different areas of the porous ultrathin Nd_2O_3 nanosheets. (**E**) Low-resolution TEM image of the porous Nd_2O_3 nanosheets; the inset shows the corresponding magnified image of the low-resolution TEM image. (**F**) HRTEM image of the porous ultrathin Nd_2O_3 nanosheets and inset image of the corresponding FFT patterns. (**G**) AFM characterizations of the porous ultrathin Nd_2O_3 nanosheets. (**H**) Diagram of periodic table of elements. The metal (pink) oxides are prepared by the expansion method. Scale bars: (C and D) 1 μm, (E) 1 μm and (inset) 100 nm, (F) 2 nm and (inset) 2 1/nm, and (G) 1 μm.

electron microscopy (TEM) images (Fig. 1E), the Nd_2O_3 nanosheet has a porous structure with an average pore size of about 100 nm. In addition, the thickness of the single Nd_2O_3 porous nanosheet is about 2 nm through the measurement of atomic force microscopy (AFM) (Fig. 1G). The x-ray diffraction (XRD) pattern (fig. S1) reveals that the ultrathin Nd_2O_3 porous nanosheet belongs to the A-type hexagonal structure (*34*), which is verified by the high-resolution TEM (HRTEM) image and fast Fourier transform (FFT) image pattern with a positive hexagonal dot matrix (Fig. 1F, inset). Electron diffraction pattern shows polycrystalline rings (fig. S2), suggesting that the nanosheet is formed by cross-linking single-crystal particles. Figure 1H shows the elements in the periodic table, whose oxides have been prepared using this method.

In addition to Nd_2O_3, the Sm_2O_3, Gd_2O_3, Er_2O_3, CeO_2, Pr_4O_7, and Yb_2O_3 ultrathin porous nanosheets could also be prepared by substituting $Nd(NO_3)_3 \cdot 6H_2O$ with the corresponding metal salts.

SEM and low-magnification TEM images demonstrate that the rare-earth metal oxide nanosheets are transparent, flexible, and curled, just like muslin. The transverse dimension of rare-earth metal oxide nanosheets reaches about 50 μm, with the thickness being less than 5 nm (Fig. 2 and fig. S3). In addition, a statistical analysis of pore sizes of different rare-earth oxides indicates that the pore sizes of most ultrathin porous rare-earth oxide nanosheets distribute mainly in about 10 nm except Er_2O_3 ultrathin nanosheets, whose pore sizes varies from 40 to 80 nm. By the way, the content of precursors can easily control the pore size and thickness of these nanosheets. The increased precursor content results in the reduction in the pore size and the increase in the nanosheets' thickness (Fig. 2 and fig. S4). The HRTEM images and the corresponding FFT patterns, selected-area electron diffraction (SAED) patterns (fig. S1), and XRD patterns (fig. S2) verify the structures of rare-earth oxides, indicative of Sm_2O_3, Gd_2O_3, Er_2O_3, and Yb_2O_3 with the C-type cubic bixbyite structure and CeO_2
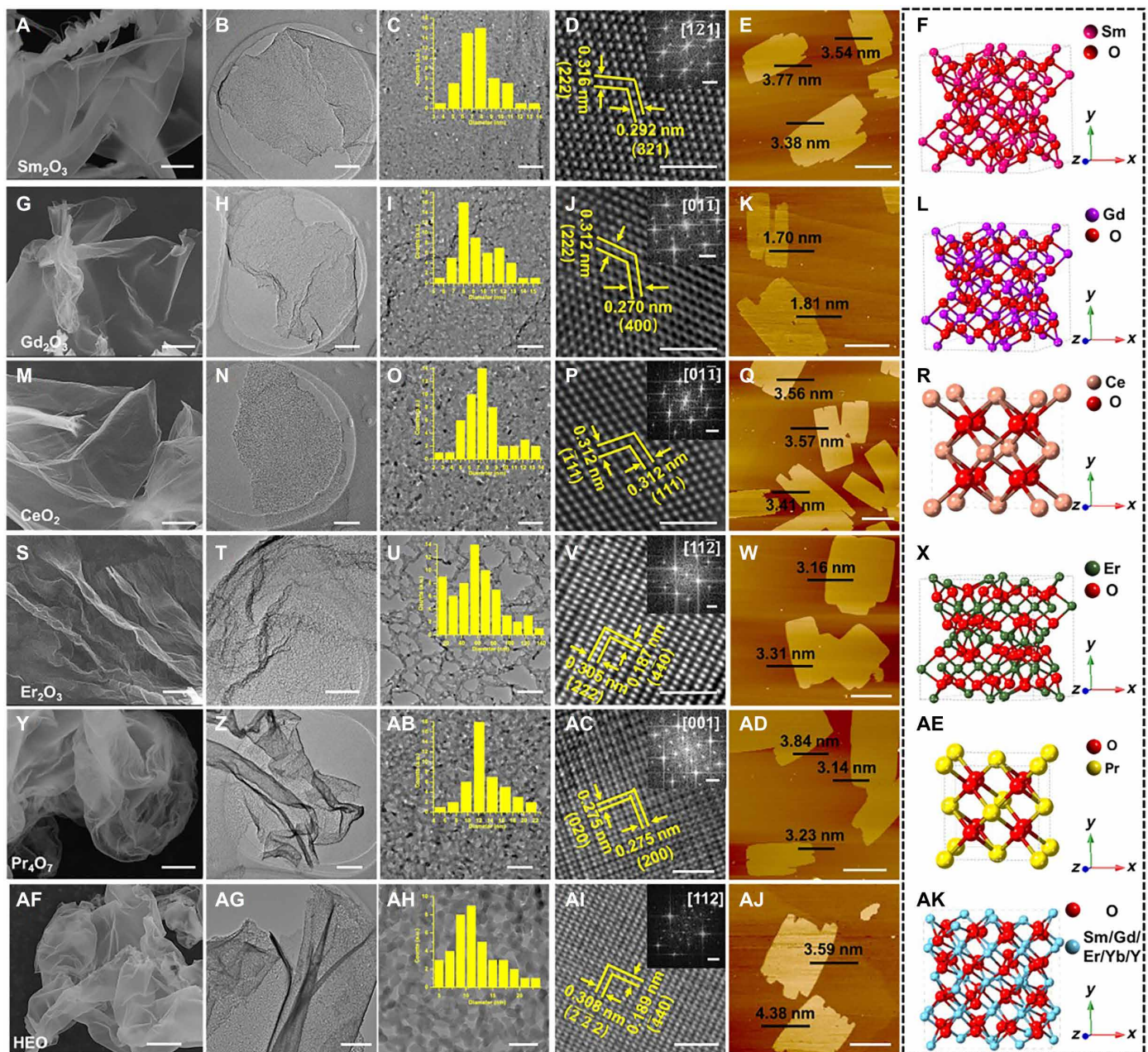
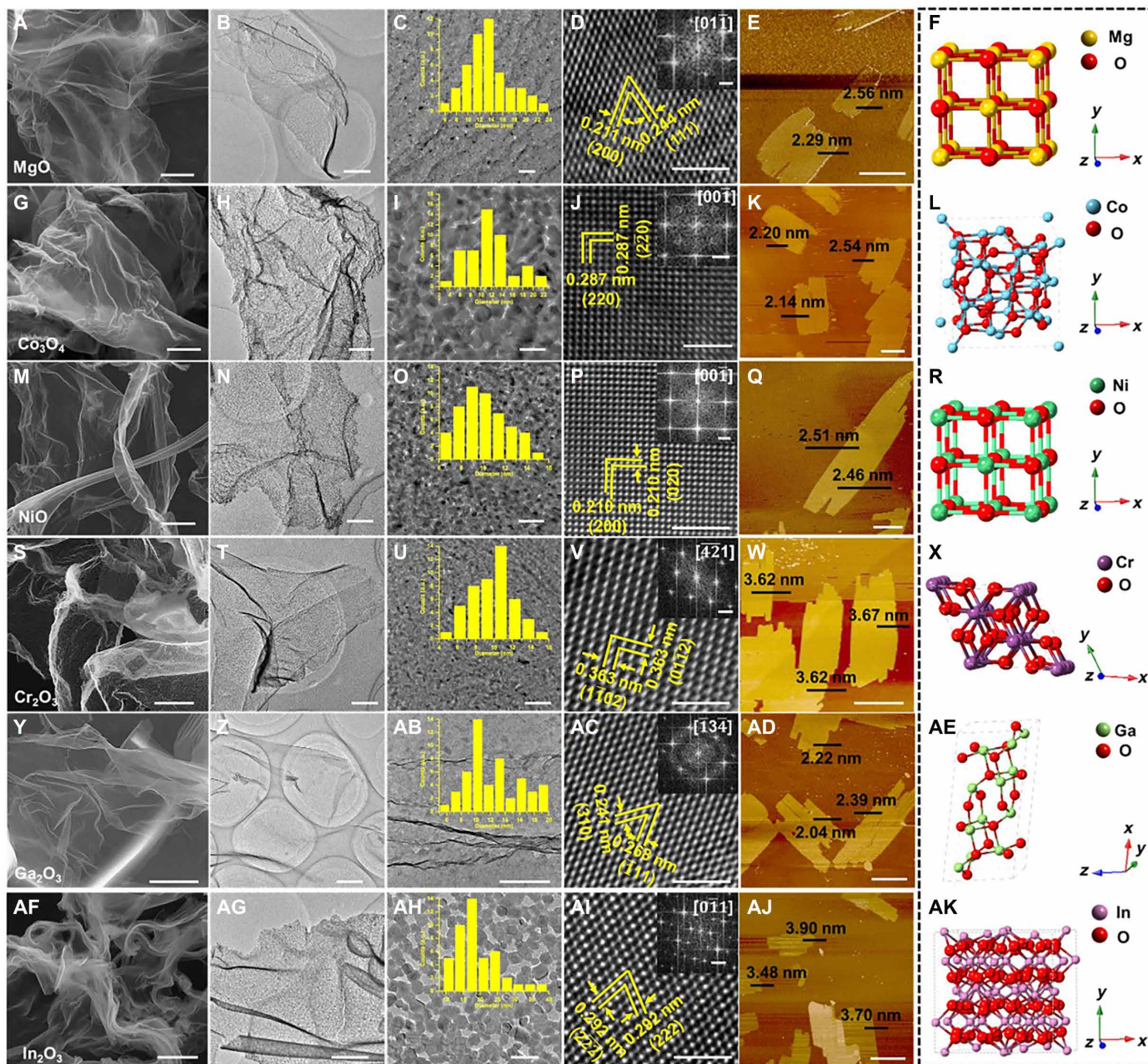**Fig. 2. Characterizations of rare-earth oxides.** (**A**, **G**, **M**, **S**, **Y**, and **AF**) SEM images. (**B**, **H**, **N**, **T**, **Z**, and **AG**) TEM images. (**C**, **I**, **O**, **U**, **AB**, and **AH**) Magnified TEM images and inset images of the pore size distributions. (**D**, **J**, **P**, **V**, **AC**, and **AI**) HRTEM images and inset images of the corresponding FFT patterns. (**E**, **K**, **Q**, **W**, **AD**, and **AJ**) AFM images. Atomic structures of Sm_2O_3 (**F**), Gd_2O_3 (**L**), CeO_2 (**R**), Er_2O_3 (**X**), Pr_4O_7 (**AE**), and HEO of $(ErGdYbSm_{1.2}Y_{0.8})_2O_3$ (**AK**). Scale bars: (A, G, M, S, Y, and AF) 5 μm, (B, H, N, T, and Z) 1 μm, (AG) 500 nm, (C, I, O, U, and AB) 100 nm, (AH) 50 nm, (D, J, P, V, AC, and AI) 2 nm and (inset) 2 1/nm, (E, K, Q, AD, and AJ) 2 μm, and (W) 1 μm.

and Pr_4O_7 with the cubic fluorite structure; the corresponding atomic structures are shown in Fig. 2 (F, L, R, X, AE, and AK) (*34–36*). It is worth mentioning that high-entropy oxides (HEOs) (*37–39*) of $(ErGdYbSm_{1.2}Y_{0.8})_2O_3$ and $(CoMnNiCrFe)_3O_4$ with unique structural characteristics were also prepared by this method. As shown in Fig. 2 and figs. S2, S5, and S6, $(ErGdYbSm_{1.2}Y_{0.8})_2O_3$ and $(CoMnNiCrFe)_3O_4$ remain the single phase of the C-type cubic bixbyite structure and the single phase of the spinel structure, respectively. Besides, the morphology of HEO displays an ultrathin porous structure assembled by nanoparticles. According to the energy-dispersive spectroscopy

(EDS) spectrum and elemental mapping, the statistical distribution and content of cation are almost identical, further verifying the characteristics of the HEOs (fig. S6). In addition, diverse monometallic oxide ultrathin nanosheets can be targeted by replacing rare-earth metal element with alkaline-earth metal elements, transition metal elements, and III-main group metal elements. The resulting library of monometallic oxide ultrathin porous nanosheets is presented in Fig. 3 and fig. S8. Three classes of oxides—such as alkaline earth metal oxide MgO; transition metal oxides Co_3O_4, Mn_3O_4, NiO, Cr_2O_3, ZrO_2, and α-Fe_2O_3; and III-main group oxides Al_2O_3, Ga_2O_3, and

Fig. 3. Characterizations of II-main group, transition metal, and III-main group metal oxides. (**A**, **G**, **M**, **S**, **Y**, and **AF**) SEM images. (**B**, **H**, **N**, **T**, **Z**, and **AG**) TEM images. (**C**, **I**, **O**, **U**, **AB**, and **AH**) Magnified TEM images and inset images of the pore size distributions. (**D**, **J**, **P**, **V**, **AC**, and **AI**) HRTEM images and inset images of the corresponding FFT patterns. (**E**, **K**, **Q**, **W**, **AD**, and **AJ**) AFM images. Atomic structures of MgO (**F**), Co_3O_4 (**L**), NiO (**R**), Cr_2O_3 (**X**), Ga_2O_3 (**AE**), and In_2O_3 (**AK**). Scale bars: (A, G, M, S, Y, and AF) 5 μm, (B, H, N, T, Z, and AG) 1 μm, (C, I, O, U, AB, and AH) 100 nm, (D, J, P, V, AC, and AI) 2 nm and (inset) 2 1/nm, and (E, K, Q, W, AD, and AJ) 1 μm.

In_2O_3—have the similar morphology as large-area curled porous nanosheets assembled by nanoparticles. The corresponding thickness of above oxides is about 3 to 4 nm characterized by AFM. The structure of monometallic oxides is confirmed by XRD, HRTEM, and SAED measurements (Fig. 3 and figs. S7, S8, and S10), indicating the cubic structure of MgO, NiO, In_2O_3, and Al_2O_3; the spinel structure of Co_3O_4 and Mn_3O_4; the corundum structure of Cr_2O_3 and α-Fe_2O_3; the monoclinic structure of Ga_2O_3; and the mixture of monoclinic and tetragonal structures of ZrO_2. In addition to monometallic oxides,

ultrathin porous nanosheets of $CaCO_3$ and $SrCO_3$ can be prepared by this method as well (fig. S9).

This method can be extended to prepare ultrathin perovskite oxides by replacing monometallic nitrates with two mixing metal nitrates in a predetermined ratio. Single perovskite has a common formula of ABX_3, in which A is rare-earth metal ion and B is transition metal ion, and has four common space groups such as *Pnma*, Pm$\bar{3}$m, *I*4, and *R*$\bar{3}$*c* (*40*, *41*). Through cations of A and B exchange with different rare-earth metal ion and transition metal ion, various

large-size ultrathin perovskite oxides were also prepared, including $La_{0.96}Mn_{0.96}O_3$ (LMO), $LaNiO_3$ (LNO), $LaCoO_3$ (LCO), LFO, $GdCoO_3$ (GCO), $GdMnO_3$ (GMO), and $GdFeO_3$ (GFO), further indicating the universality of the method (Fig. 4 and figs. S11 to S13). XRD analysis (figs. S9 and S11) of the library of single perovskites indicates the hexagonal structure of LMO ($a = 5.5188$ Å, $c = 13.3100$ Å) and LNO ($a = 5.4573$ Å, $c = 13.1462$ Å), the rhombohedral structure of LCO ($a = 5.3778$ Å, $\alpha = 60.7980$ Å), and the orthorhombic structure of LFO ($a = 5.5530$ Å, $b = 5.5630$ Å, $c = 7.8670$ Å), GCO ($a = 5.5530$ Å, $b = 5.5630$ Å, $c = 7.8670$ Å), GMO ($a = 5.3100$, $b = 5.8400$, $c = 7.4300$),

and GFO ($a = 5.3497$ Å, $b = 5.6107$ Å, $c = 7.6676$ Å), which confirm that the perovskites with the larger A ion radii such as La^{3+} tend to form a hexagonal structure, while smaller ion radii such as Gd^{3+} are more likely to form an orthorhombic structure (40). The HRTEM images and the corresponding FFT patterns further confirm the structure of single perovskites. The corresponding atomic structures are shown in Fig. 4. By adding additional transition metal elements, we have synthesized double perovskite oxides [$LaFe_{0.75}Ni_{0.25}O_3$ (LFNO), $LaCo_{0.5}Ni_{0.5}O_3$ (LCNO), $LaCo_{0.5}Mn_{0.5}O_3$ (LCMO), $LaNi_{0.5}Mn_{0.5}O_3$ (LNMO), Gd_2CoMnO_6 (GCMO), $Gd(Fe_{0.6}Mn_{0.4})O_3$
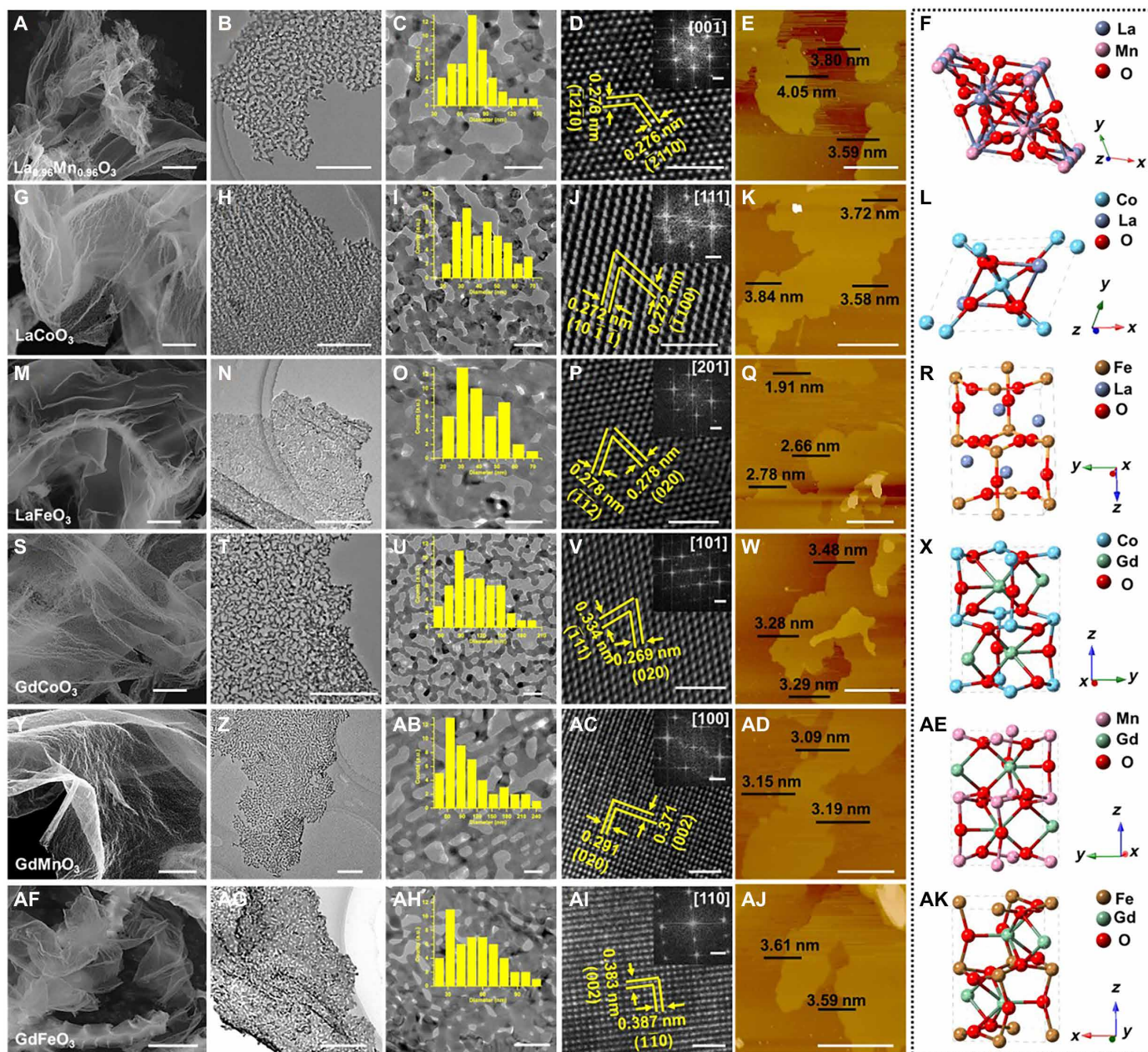
Fig. 4. Characterizations of single perovskites. (**A**, **G**, **M**, **S**, **Y**, and **AF**) SEM images. (**B**, **H**, **N**, **T**, **Z**, and **AG**) TEM images. (**C**, **I**, **O**, **U**, **AB**, and **AH**). Magnified TEM images and inset images of the pore size distributions. (**D**, **J**, **P**, **V**, **AC**, and **AI**) HRTEM images and inset images of the corresponding FFT patterns. (**E**, **K**, **Q**, **W**, **AD**, and **AJ**) AFM images. Atomic structures of LMO (**F**), LCO (**L**), LFO (**R**), GCO (**X**), GMO (**AE**), and GFO (**AK**). Scale bars: (A, G, M, S, Y, and AF) 5 μm, (B, H, N, T, Z, and AG) 1 μm, (C, I, O, U, AB, and AH) 100 nm, (D, J, P, V, AC, and AI) 2 nm and (inset) 2 1/nm, and (E, K, Q, W, AD, and AJ) 1 μm.

(GFMO), and Gd(Co$_{0.5}$Fe$_{0.5}$)O$_3$ (GCFO)] and triple perovskite oxides [La(Mn$_{0.33}$Ni$_{0.33}$Co$_{0.33}$)O$_3$ (LMNCO), La(Mn$_{0.3}$Fe$_{0.4}$Co$_{0.3}$)O$_3$ (LMFCO), and La(Co$_{0.33}$Ni$_{0.33}$Fe$_{0.33}$)O$_3$ (LCNFO)], and the thicknesses of these oxide nanosheets are all less than 5 nm according to the AFM characterizations (Fig. 5). Furthermore, the corresponding EDS spectrums and elemental mapping of the double/triple perovskite oxides demonstrate the uniformity of metal elemental distributions, thus confirming that this method can prepare homogeneous double/triple perovskite oxides (Fig. 5, figs. S14 to 20). The phase structures of the double/triple perovskite oxides are further revealed by XRD, refinement XRD, and HRTEM (Fig. 5 and figs. S17, S19, and S20). The atomic structures of double/triple perovskites can be classified into three types: LFNO, GCMO, GFMO, GCFO, LMNCO, LMFCO, and LCNFO ultrathin porous nanosheets with an orthorhombic structure; LCMO ultrathin porous nanosheet with a monoclinic structure (a = 5.52464 Å, b = 5.48302 Å, c = 7.7717 Å, β = 89.89°); and LNMO (a = 5.5042 Å, b = 5.5042 Å, c = 13.2369 Å) and LCNO (a = 5.464 Å,

b = 5.464 Å, c = 13.125 Å) porous nanosheets with hexagonal structures. The stoichiometry of multimetallic oxides can be controlled effectively via this method. The double perovskite LaFe$_x$Ni$_{1-x}$O$_3$ (LFNO) porous nanosheets (x = 0.25, 0.5, and 0.75 and denoted as LFNO-I, LFNO-II, and LFNO-III, respectively) were prepared by regulating the ratio of nickel nitrate and iron nitrate precursors. As shown in fig. S21, the element distributions of LFNO-I, LFNO-II, and LFNO-III confirm that the various stoichiometry of multimetallic oxides can be successfully prepared. To further characterize the structure of LFNO, Rietveld XRD patterns were carried out. LFNO-I is consistent with the hexagonal perovskite structure, while LFNO-II and LFNO-III confirm the single phase of the orthorhombic perovskite structure (fig. S22). The corresponding structural parameters calculated by the Rietveld refinements are shown in table S3. Besides, the surface area and pore sizes of 2D representative oxide nanosheets were evaluated on the basis of the nitrogen adsorption isotherms by using the Brunauer-Emmett-Teller (BET)
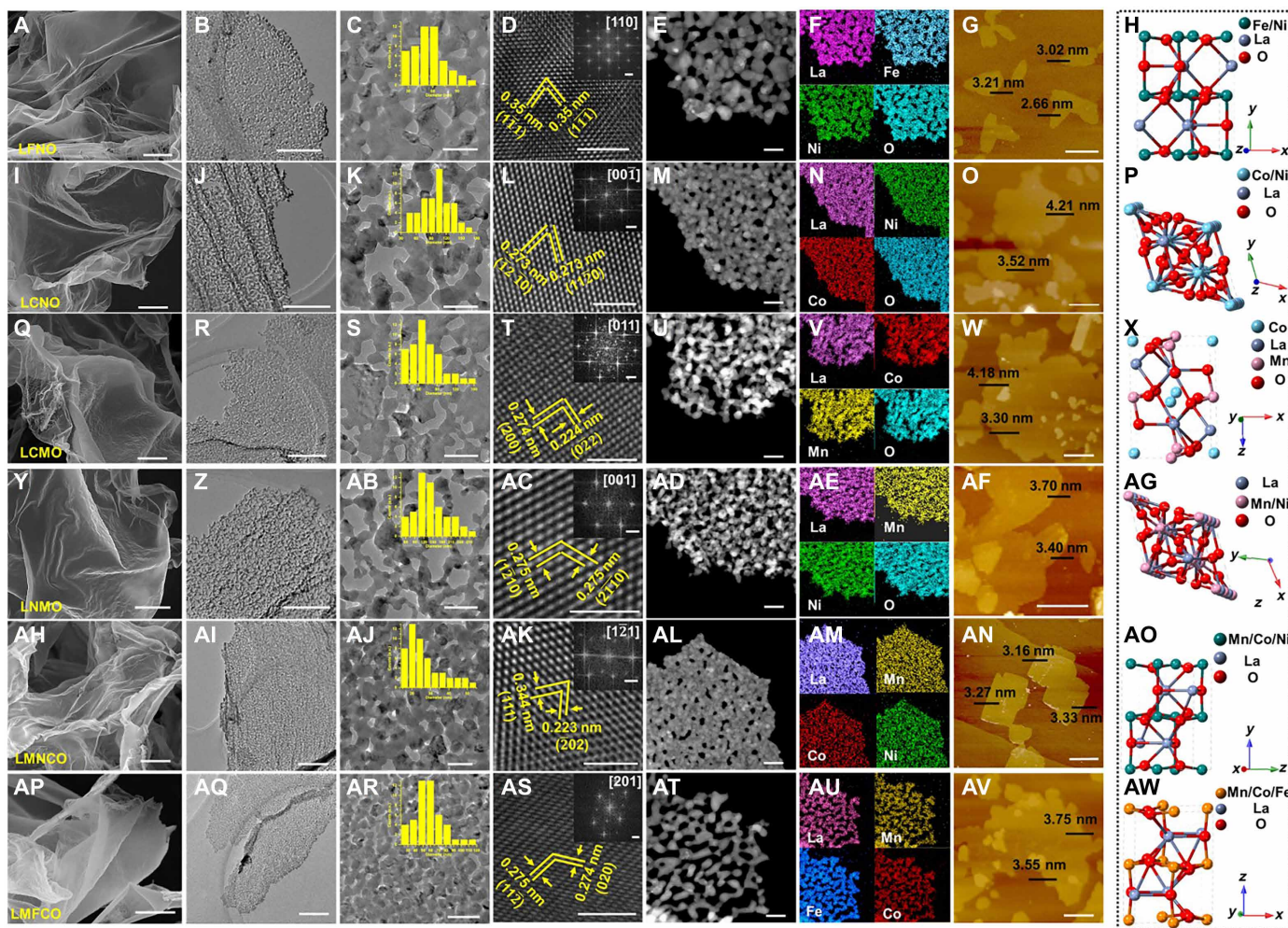

Fig. 5. Characterizations of double and triple perovskites. (**A**, **I**, **Q**, **Y**, **AH**, and **AP**) SEM images. (**B**, **J**, **R**, **Z**, **AI**, and **AQ**) TEM images. (**C**, **K**, **S**, **AB**, **AJ**, and **AR**) Magnified low-resolution TEM images and inset images of the pore size distributions. (**D**, **L**, **T**, **AC**, **AK**, and **AS**) HRTEM images and inset images of the corresponding FFT patterns. (**E** and **F**, **M** and **N**, **U** and **V**, **AD** and **AE**, **AL** and **AM**, and **AT** and **AU**) high angle angular dark field–scanning transmission electron microscopy (HADDF-STEM) images and corresponding elemental mapping. (**G**, **O**, **W**, **AF**, **AN**, and **AV**) AFM images. Atomic structures of LFNO (**H**), LCNO (**P**), LCMO (**X**), LNMO (**AG**), LMNCO (**AO**), and LMFCO (**AW**). Scale bars: (A, I, Q, Y, AH, and AP) 5 μm, (B, J, R, Z, AI, and AQ) 1 μm, (C, K, S, AB, AJ, and AR) 100 nm, (D, J, P, V, AC, and AI) 2 nm and (inset) 2 1/nm, (E and F, M and N, U and V, AD and AE, AL and AM, and AT and AU) 100 nm, and (G, O, W, AF, AN, and AV) 1 μm.

method and the Barrett-Joyner-Halenda (BJH) pore size analysis. The surface area is ~60, ~54, ~40, ~38, ~45, and ~77 m^2/g for the samples of MgO, Cr_2O_3, GFO, LCO, LMNCO, and Gd_2O_3, respectively (fig. S23). The BJH pore size distributions (fig. S23) show peaks at the mesopore widths at about 13 nm (MgO), 11 nm (Cr_2O_3), 30 nm (GFO), 35 nm (LCO), 20 nm (LMNCO), and 8 nm (Gd_2O_3), which are consistent with the values obtained from the TEM images. It is worth noting that the oxide nanosheets showed a sharp peak corresponding to mesopores with an average size of 3 to 4 nm, which originates from the house-of-cards–type stacking structure of sheet-like crystallinity (*15*).

Mechanisms for the synthesis of ultrathin porous oxide nanosheets

We then investigate the synthesis mechanism of as-prepared ultrathin porous oxide nanosheets using the typical sample of Y_2O_3. To study the details of the synthesis process, we annealed the mixture of 0.4 g of glucose, 0.5 g of ammonium nitrate, and 0.02 g of yttrium nitrate at 500°C from 10 s to 5 min (Fig. 6A and movie S2). The reaction process of glucose and ammonium nitrate was tracked using thermogravimetric analysis–derivative thermogravimetry (TGA-DTG) (Fig. 6B). The thermogravimetric profile of glucose shows three endothermic peaks corresponding to its melting, condensation, and
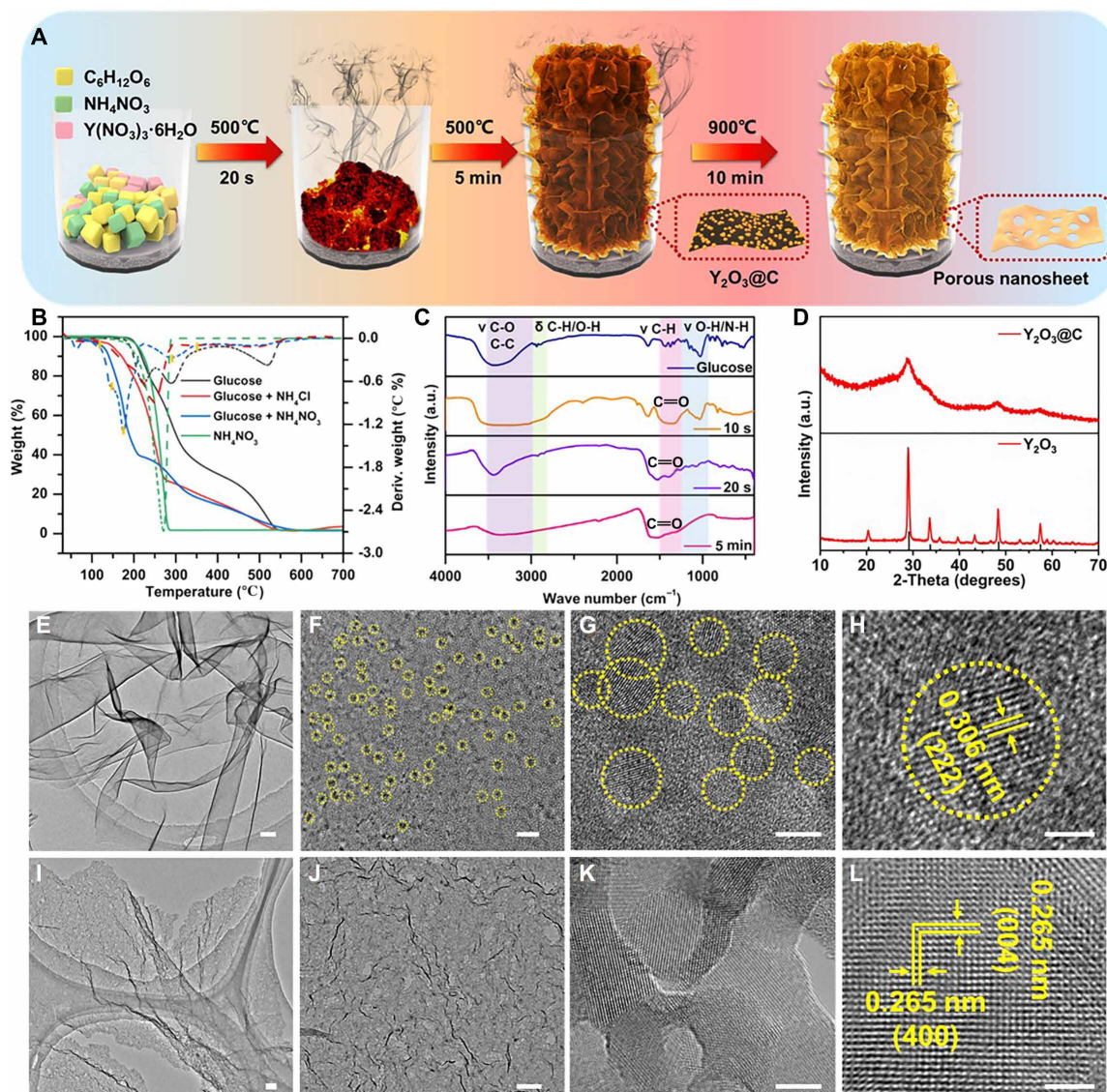
Fig. 6. Synthesis mechanism of ultrathin porous oxide nanosheets. (**A**) Schematics of the reaction mechanism for the synthesis of Y_2O_3 nanosheets. (**B**) TGA-DTG curves of glucose, glucose-NH_4Cl mixture, glucose-NH_4NO_3 mixture, and NH_4NO_3 with temperature up to 700°C at a heating rate of 10°C/min in O_2 atmosphere. (**C**) FTIR spectrums of glucose and glucose-NH_4NO_3-$Y(NO_3)_3$·6H$_2$O mixture annealed at 500°C for 10 s, 20 s, and 5 min. (**D**) XRD of Y_2O_3@C nanosheet and Y_2O_3 porous nanosheet. Low-resolution TEM images of Y_2O_3@C nanosheet (**E**) and Y_2O_3 porous nanosheet (**I**). Scale bars: (E and I) 100 nm. Magnified low-resolution TEM images of Y_2O_3@C nanosheet (**F** and **G**) and Y_2O_3 porous nanosheet (**J** and **K**). Scale bars: (F and J) 20 nm and (G and K) 5 nm. HRTEM images of Y_2O_3@C nanosheet (**H**) and Y_2O_3 porous nanosheet (**L**). Scale bars: (H and L) 2 nm.

polymerization. The pyrolysis process of the mixture of glucose and ammonium nitrate is different from that of glucose. The weight loss of the mixture at 120°C corresponds to the water loss during the condensation of aldohexose and ammonia. The strong heat absorption peak at 143°C is assigned to the melting process, followed by a series of heat absorption peaks (143° to 175°C), corresponding to the second step of the Maillard reaction. In addition, the endothermic peak of the mixture of glucose and ammonium nitrate is lower than that of the mixture of glucose and ammonium chloride, indicating that the nitrate ions provide an oxidizing environment to accelerate the deamination and dehydration of the intermediates. Further pyrolysis of the Maillard product and glucose at 285°C led to the partial formation of carbon materials. Figure 6C shows the Fourier transform infrared (FTIR) spectrometer profiles of glucose and the mixture of glucose, ammonium nitrate, and yttrium nitrate at different reaction times. When the mixture under heating at 500°C for 10 s, the absorption centered at 1640 cm^{-1} corresponding to C=O stretching is observed, implying the transformation to various carbonyls. In addition, the weakening of the O—H/N—H stretching vibration compared to that of glucose further demonstrates the reaction of deamination and dehydration corresponding to the second stage of the Maillard reaction (42). After heating the mixture for 20 s, the featured absorption of C=O stretching continuously becomes stronger, suggesting that more carbonyl groups are accumulated and the sticky Melanoidin polymers have been formed. This reaction process corresponds to the advanced stage of Maillard reaction (movie S2) (31, 32, 42). The sticky Melanoidin polymers with sufficient oxygen-contained groups such as carboxyl and hydroxyl could chelate with various oxide precursors (10, 43). By heating the mixture at 500°C for 5 min, the Melanoidin polymer has a violent redox reaction to nitrate ions, so the polymer interior expands rapidly, forming large-size ultrathin carbon nanosheets, while the ultrasmall Y_2O_3 nanoparticle particles are embedded in the carbon nanosheet (eq. S2-1). After that, Y_2O_3@C nanosheets are annealed at 900°C to obtain Y_2O_3 ultrathin porous nanosheets (Fig. 6, I to L). In this process, the large-size carbon nanosheets are highly flexible, which contributes to maintaining the structure stability of porous nanosheets during high-calcination temperature. The oxide nanoparticles can grow laterally and chemically linked with each other to form porous nanosheets in the calcination process. By XRD and TEM analysis, the amorphous carbon decomposes completely, and the metal oxide nanoparticles grow and sinter together, forming particle-assembled ultrathin porous oxide nanosheets (eq. S2-2). We speculate that the generation of ultrathin porous metal oxide nanosheets occurs via the following three steps: First, the ammonium ions and glucose undergo a Maillard reaction to form a sticky Melanoidin polymer with sufficient oxygen-containing functional groups such as carboxyl, hydroxyl, and epoxy groups, which ensure adsorption of versatile oxide precursors. Second, the Melanoidin polymer participates in a violent redox reaction with nitrate ions, and the inner part of the polymer expands rapidly, forming large-size ultrathin carbon nanosheets. Besides, the oxide precursors decompose to oxide nanoparticles, which are embedded in the carbon nanosheet. In the post-calcination process, the oxide nanoparticles are connected with each other through orientated attachment and coalescence growth to form porous oxide nanosheets by using large-size ultrathin carbon nanosheets as a template. To further confirm the role of self-sacrificing templates, Y_2O_3, Co_3O_4, and MgO were synthesized by annealing the corresponding metal nitrates without glucose and ammonium nitrate. The SEM images of Co_3O_4 and MgO show that the

morphologies of those two samples are particles with a size of ~1 μm, and the SEM image of Y_2O_3 shows the thick plate morphology (fig. S24). No ultrathin oxide nanosheet is observed. Moreover, the template is fabricated by calcining the ammonium nitrate and glucose without metal precursor at 500°C for 10 min. As shown in fig. S25, ultrathin large-size carbon nanosheets can be observed in the SEM and TEM images. To explore the effect on nitrate and ammonium ions, we annealed glucose and glucose with different ammonium salts, such as ammonium sulfate, ammonium acetate, and ammonium chloride, at 500°C for 5 min. According to the SEM images (figs. S25 and S26, A to D), only the reaction of glucose with ammonium nitrate can produce large-size carbon nanosheets, while annealing other mixtures only produces plate-like carbon materials. Besides, directly calcining the mixture of yttrium nitrate and glucose tends to form a 3D porous structure of Y_2O_3 (fig. S26E).

Electrocatalytic OER activity of ultrathin porous perovskite oxide nanosheets

The as-prepared ultrathin perovskite oxides with high surface areas display great electrocatalytic activity for OER. Several perovskite oxides, including LCO, LFO, LMO, GCO, GMO, and GFO, were then evaluated in a conventional three-electrode electrochemical system in 1 M KOH electrolyte with a Hg/HgO reference electrode. Figure S27A shows the OER polarization curves obtained from linear sweep voltammetry measurements. Obviously, LFO has the highest catalytic activity, the lowest onset potential (~112.55 mV), and the smallest overpotential (~303.52 mV) at the current density of 10 mA cm^{-2} among the samples studied (fig. S27, B and C). This value is also comparable or superior to recently reported perovskite-based catalysts (table S4) (44–56). The mass activity of LFO at 1.55 V [versus (reversible hydrogen electrode) RHE] reaches 18.21 A g$^{-1}_{oxide}$, which is also better than those of LMO (8.48 A g$^{-1}_{oxide}$), GFO (7.60 A g$^{-1}_{oxide}$), LCO (5.20 A g$^{-1}_{oxide}$), GMO (5.17 A g$^{-1}_{oxide}$), and GCO (4.20 A g$^{-1}_{oxide}$) (fig. S27D). The results suggest that the electrocatalytic activity increases with the ionic radius of the A-site cation. The specific activity and turnover frequency (TOF) of LFO are 0.0058 mA cm$^{-2}_{oxide}$ (fig. S27E) and 0.02438 S^{-1} (fig. S27F) at a potential of 1.55 V versus RHE, respectively, further verifying that LFO has more accessible active sites. Besides, LFO has a higher double-layer capacitance (C_{dl}) of 17.6 mF cm^{-2}, as estimated from cyclic voltammetry (fig. S28). The catalytic kinetics of the perovskite samples assessed from Tafel plots in 1 M KOH solution shows that LFO has the best kinetic activity with a Tafel slope of about 63.6 mV dec^{-1} (fig. S27G) among the samples studied. According to the chronopotentiometric measurements at a current density of 10 mA cm$^{-2}_{disk}$, LFO has a stable electrocatalytic performance, retaining 92% of the initial current density after 30,000 s (fig. S27H).

DISCUSSION

In conclusion, we have developed a universal strategy for fabrication of ultrathin oxide nanosheets by a self-formed sacrificial carbon template. The growth of carbon template mainly depends on the Maillard reaction between ammonium nitrate and glucose, and the following puffing process. We have successfully fabricated 36 different kinds of oxide nanosheets using this method, including rare-earth oxides, transition metal oxides, III-main group oxides, II-main group oxides, complex perovskite oxides, and HEOs. The as-obtained ultrathin perovskite oxides demonstrate remarkable electrocatalytic activity

for OER. This synthesis method for ultrathin oxide nanosheets is simple, efficient, and cost-effective, thus holding great potential for industrial application.

MATERIALS AND METHODS
Synthesis of ultrathin porous nanosheet
Synthesis of 2D rare-earth oxides
In the synthesis of 2D Pr_4O_7, 0.4 g of glucose, 0.5 g of ammonium nitrate, and 0.02 g of praseodymium nitrate hexahydrate were ground well in a mortar, and then the ground powder was placed in a crucible and heated up to 900°C for 10 min in the muffle furnace. The 2D Pr_4O_7 was obtained without the purging process when the furnace cooled down to room temperature. Other 2D porous rare-earth oxides (Nd_2O_3, Sm_2O_3, Gd_2O_3, Er_2O_3, Yb_2O_3, Y_2O_3, and CeO_2 nanosheets) were prepared similarly by replacing praseodymium nitrate hexahydrate with neodymium nitrate hexahydrate, samarium nitrate hexahydrate, gadolinium nitrate hexahydrate, erbium nitrate pentahydrate, ytterbium nitrate pentahydrate, yttrium nitrate hexahydrate, and cerium nitrate pentahydrate.

Synthesis of 2D transition oxides
Taking the synthesis of 2D ZrO_2 as an example, 0.4 g of glucose, 0.5 g of ammonium nitrate, and 0.02 g of zirconium nitrate pentahydrate were ground well in a mortar, and then the ground powder was heated up to 900°C for 10 min in the muffle furnace. The 2D ZrO_2 was obtained without the purging process when the furnace cooled down to room temperature. Other ultrathin transition oxide nanosheets (Cr_2O_3, Mn_3O_4, Fe_2O_3, Co_3O_4, and NiO) were prepared similarly by using the precursor of chromium nitrate, manganese nitrate tetrahydrate, ferric nitrate nine-hydrate, cobalt chloride hexahydrate, and nickel nitrate hexahydrate, respectively, and lowering the annealing temperature to 500°C for 20 min.

Synthesis of 2D porous II-main group metal oxides and carbonates
In the synthesis of 2D MgO, 0.4 g of glucose, 0.5 g of ammonium nitrate, and 0.02 g of magnesium nitrate were ground well in a mortar, and then the ground powder was heated up to 500°C for 20 min in the muffle furnace. The 2D MgO was obtained without the purging process when the furnace cooled down to room temperature. Other ultrathin metal carbonate nanosheets ($CaCO_3$ and $SrCO_3$) were prepared similarly by using the precursor of calcium nitrate tetrahydrate and strontium nitrate, respectively, and the annealing time is reduced to 10 min.

Synthesis of 2D porous III-main group metal oxides
In the synthesis of 2D Al_2O_3, 0.4 g of glucose, 0.5 g of ammonium nitrate, and 0.02 g of aluminum nitrate were ground well in a mortar, and then the ground powder was heated up to 900°C for 10 min in the muffle furnace. The 2D Al_2O_3 was obtained without the purging process when the furnace cooled down to room temperature. Other ultrathin III-main group metal oxide nanosheets (Ga_2O_3 and In_2O_3) were prepared similarly by using the precursor of gallium nitrate and indium nitrate, respectively, and lowering the annealing temperature to 500°C for 20 min.

Synthesis of lanthanide-based perovskite oxides
In the synthesis of 2D LMO, 0.4 g of glucose, 0.5 g of ammonium nitrate, 0.022 g of lanthanum nitrate hexahydrate, and 0.022 g of manganese nitrate tetrahydrate were ground well in a mortar, and then the ground powder was placed in a crucible and heated up to 700°C for 20 min in the muffle furnace. The 2D LMO was obtained without the purging process when the furnace cooled down to room temperature. Other 2D porous lanthanide-based perovskite oxide nanosheets (LFO, LCO, and LNO) are prepared similarly by replacing manganese nitrate tetrahydrate with ferric nitrate nine-hydrate, cobalt nitrate hexahydrate, and nickel nitrate hexahydrate.

Synthesis of lanthanide-based double perovskite oxides
In the synthesis of 2D $LaMn_{0.5}Ni_{0.5}O_3$, 0.4 g of glucose, 0.5 g of ammonium nitrate, 0.022 g of lanthanum nitrate hexahydrate, 0.0063 g of manganese nitrate tetrahydrate, and 0.0072 g of nickel nitrate hexahydrate were ground well in a mortar, and then the ground powder was placed in a crucible and heated up to 700°C for 20 min in the muffle furnace. The 2D $LaMn_{0.5}Ni_{0.5}O_3$ was obtained without the purging process when the furnace cooled down to room temperature. Other 2D porous lanthanide-based perovskite oxide nanosheets ($LaMn_{0.5}Co_{0.5}O_3$, LCNO, and LFNO) are prepared similarly by replacing manganese nitrate tetrahydrate and nickel nitrate hexahydrate with the corresponding equimolar ratio of transition metal nitrates.

Synthesis of lanthanide-based triple perovskite oxides
Taking 2D LMNCO as an example, 0.4 g of glucose, 0.5 g of ammonium nitrate, 0.022 g of lanthanum nitrate hexahydrate, 0.0042 g of manganese nitrate tetrahydrate, 0.0048 g of cobalt nitrate hexahydrate, and 0.0048 g of nickel nitrate hexahydrate were ground well in a mortar, and then the ground powder was placed in a crucible and heated up to 700°C for 20 min in the muffle furnace. The 2D LMNCO was obtained without the purging process when the furnace cooled down to room temperature. The 2D porous LMFCO nanosheets are prepared similarly by replacing nickel nitrate hexahydrate with ferric nitrate nine-hydrate. The 2D porous LCNFO nanosheets are prepared similarly by replacing manganese nitrate tetrahydrate with ferric nitrate nine-hydrate.

Synthesis of gadolinium-based perovskite oxides
Taking 2D GMO as an example, 0.4 g of glucose, 0.5 g of ammonium nitrate, 0.022 g of gadolinium nitrate hexahydrate, and 0.022 g of manganese nitrate tetrahydrate were ground well in a mortar, and then the ground powder was placed in a crucible and heated up to 900°C for 20 min in the muffle furnace. The 2D GMO was obtained without the purging process when the furnace cooled down to room temperature. Other 2D porous gadolinium-based perovskite oxide nanosheets (GFO and GCO) are prepared similarly by replacing manganese nitrate tetrahydrate with ferric nitrate nine-hydrate and cobalt nitrate hexahydrate.

Synthesis of gadolinium-based double perovskite oxides
Taking 2D GCMO as an example, 0.4 g of glucose, 0.5 g of ammonium nitrate, 0.022 g of gadolinium nitrate hexahydrate, 0.0063 g of manganese nitrate tetrahydrate, and 0.0072 g of cobalt nitrate hexahydrate were ground well in a mortar, and then the ground powder was placed in a crucible and heated up to 900°C for 20 min in the muffle furnace. The 2D GCMO was obtained without the purging process when the furnace cooled down to room temperature. The 2D porous GFMO nanosheets are prepared similarly by replacing cobalt nitrate hexahydrate with ferric nitrate nine-hydrate. The 2D porous GCFO nanosheets are prepared similarly by replacing manganese nitrate tetrahydrate with ferric nitrate nine-hydrate.

Synthesis of HEO
Typically, 0.4 g of glucose, 0.5 g of ammonium nitrate, 0.004 g of samarium nitrate hexahydrate, 0.004 g of gadolinium nitrate hexahydrate, 0.004 g of erbium nitrate pentahydrate, 0.004 g of ytterbium nitrate pentahydrate, and 0.004 g of yttrium nitrate hexahydrate were ground well in a mortar, and then the ground powder was placed in

a crucible and heated up to 900°C for 10 min in the muffle furnace. The 2D HEO of $(ErGdYbSm_{1.2}Y_{0.8})_2O_3$ was obtained without the purging process when the furnace cooled down to room temperature. In the synthesis of $(CoMnNiCrFe)_3O_4$, 0.4 g of glucose, 0.5 g of ammonium nitrate, 0.0033 g of chromium nitrate, 0.0034 g of manganese nitrate tetrahydrate, 0.0056 g of ferric nitrate nine-hydrate, 0.004 g of cobalt chloride hexahydrate, and 0.004 g of nickel nitrate hexahydrate were ground well in a mortar, and then the ground powder was placed in a crucible and heated up to 500°C for 20 min in the muffle furnace. The 2D HEO of $(CoMnNiCrFe)_3O_4$ was obtained without the purging process when the furnace cooled down to room temperature.

Materials characterization

The structure of the ultrathin porous oxide was characterized by XRD (X'Pert Pro, PANalytical). The morphology of the sample was observed with a field-emission SEM (FEI Nova 450 Nano and Gemini-SEM) and TEM (Tecnai G2 F30 and Titan G2 60-300). The chemical composition of the sample was analyzed using energy-dispersive x-ray spectroscopy (Gemini-SEM and Titan G2 60-300). The thickness of the nanosheets was characterized by AFM (Bruker Dimension Edge). The intermediates were characterized by thermogravimetric analyses (TGA-DTG, STA449F3), by heating from room temperature to 700°C at a rate of 10°C min^{-1} under O_2 atmosphere, and with an FTIR spectrometer (Nicolet iS50R). The surface area of the porous oxide nanosheets was investigated by measuring N_2 adsorption-desorption isotherms (ASAP 2460, adsorption gas analyzer). Before adsorption measurements, all materials were degassed by heating them at 300°C under vacuum for 10 hours.

SUPPLEMENTARY MATERIALS

Supplementary material for this article is available at https://science.org/doi/10.1126/sciadv.abn2030

REFERENCES AND NOTES

1. H. Zhang, Ultrathin two-dimensional nanomaterials. *ACS Nano* **9**, 9451–9469 (2015).
2. C. Tan, X. Cao, X. J. Wu, Q. He, J. Yang, X. Zhang, J. Chen, W. Zhao, S. Han, G. H. Nam, M. Sindoro, H. Zhang, Recent advances in ultrathin two-dimensional nanomaterials. *Chem. Rev.* **117**, 6225–6331 (2017).
3. J. E. ten Elshof, H. Yuan, P. Gonzalez Rodriguez, Two-dimensional metal oxide and metal Hydroxide nanosheets: Synthesis, controlled assembly and applications in energy conversion and storage. *Adv. Energy Mater.* **6**, 1600355 (2016).
4. G. Barcaro, A. Fortunelli, 2D oxides on metal materials: Concepts, status, and perspectives. *Phys. Chem. Chem. Phys.* **21**, 11510–11536 (2019).
5. R. Ma, T. Sasaki, Nanosheets of oxides and hydroxides: Ultimate 2D charge-bearing functional crystallites. *Adv. Mater.* **22**, 5082–5104 (2010).
6. P. Kumbhakar, C. Chowde Gowda, P. L. Mahapatra, M. Mukherjee, K. D. Malviya, M. Chaker, A. Chandra, B. Lahiri, P. M. Ajayan, A. Singh, C. S. Tiwary, Emerging 2D metal oxides and their applications. *Mater. Today* **45**, 142–168 (2021).
7. H. T. Tan, W. Sun, L. Wang, Q. Yan, 2D transition metal oxides/Hydroxides for energy-storage applications. *ChemNanoMat* **2**, 562–577 (2016).
8. J. Mei, T. Liao, L. Kou, Z. Sun, Two-dimensional metal oxide nanomaterials for next-generation rechargeable batteries. *Adv. Mater.* **29**, 1700176 (2017).
9. L. Peng, Z. Fang, Y. Zhu, C. Yan, G. Yu, Holey 2D nanomaterials for electrochemical energy storage. *Adv. Energy Mater.* **8**, 1702179 (2018).
10. D. Chen, L. Peng, Y. Yuan, Y. Zhu, Z. Fang, C. Yan, G. Chen, R. Shahbazian-Yassar, J. Lu, K. Amine, G. Yu, Two-dimensional holey Co_3O_4 nanosheets for high-rate alkali-ion batteries: From rational synthesis to in situ probing. *Nano Lett.* **17**, 3907–3913 (2017).
11. W. Xu, F. Lyu, Y. Bai, A. Gao, J. Feng, Z. Cai, Y. Yin, Porous cobalt oxide nanoplates enriched with oxygen vacancies for oxygen evolution reaction. *Nano Energy* **43**, 110–116 (2018).
12. Y. Li, F. M. Li, X. Y. Meng, S. N. Li, J. H. Zeng, Y. Chen, Ultrathin Co_3O_4 nanomeshes for the oxygen evolution reaction. *ACS Catal.* **8**, 1913–1920 (2018).
13. D. Wang, W. Zhou, R. Zhang, J. Zeng, Y. Du, S. Qi, C. Cong, C. Ding, X. Huang, G. Wen, T. Yu, Mass production of large-sized, nonlayered 2D nanosheets: Their directed

14. synthesis by a rapid "Gel-Blowing" strategy, and applications in Li/Na storage and catalysis. *Adv. Mater.* **30**, e1803569 (2018).
14. Y. Wu, T. Cao, R. Wang, F. Meng, J. Zhang, C. Cao, A general strategy for the synthesis of two-dimensional holey nanosheets as cathodes for superior energy storage. *J. Mater. Chem. A* **6**, 8374–8381 (2018).
15. K. Adpakpang, S. M. Oh, D. A. Agyeman, X. Jin, N. Jarulertwathana, I. Y. Kim, T. Sarakonsri, Y.-M. Kang, S. J. Hwang, Holey 2D nanosheets of low-valent manganese oxides with an excellent oxygen catalytic activity and a high functionality as a catalyst for $Li-O_2$ batteries. *Adv. Funct. Mater.* **28**, (2018).
16. S. S. Hong, J. H. Yu, D. Lu, A. F. Marshall, Y. Hikita, Y. Cui, H. Y. Hwang, Two-dimensional limit of crystalline order in perovskite membrane films. *Sci. Adv.* **3**, eaao5173 (2017).
17. Y. Bourlier, B. Berini, M. Fregnaux, A. Fouchet, D. Aureau, Y. Dumont, Transfer of epitaxial $SrTiO_3$ nanothick layers using water-soluble sacrificial perovskite oxides. *ACS Appl. Mater. Interfaces* **12**, 8466–8474 (2020).
18. D. Lu, D. J. Baek, S. S. Hong, L. F. Kourkoutis, Y. Hikita, H. Y. Hwang, Synthesis of freestanding single-crystal perovskite films and heterostructures by etching of sacrificial water-soluble layers. *Nat. Mater.* **15**, 1255–1260 (2016).
19. D. Li, C. Adamo, B. Y. Wang, H. Yoon, Z. Chen, S. S. Hong, D. Lu, Y. Cui, Y. Hikita, H. Y. Hwang, Stabilization of $Sr_3Al_2O_6$ growth templates for ex situ synthesis of freestanding crystalline oxide membranes. *Nano Lett.* **21**, 4454–4460 (2021).
20. D. Ji, S. Cai, T. R. Paudel, H. Sun, C. Zhang, L. Han, Y. Wei, Y. Zang, M. Gu, Y. Zhang, W. Gao, H. Huyan, W. Guo, D. Wu, Z. Gu, E. Y. Tsymbal, P. Wang, Y. Nie, X. Pan, Freestanding crystalline oxide perovskites down to the monolayer limit. *Nature* **570**, 87–90 (2019).
21. K. Yang, T. Zhang, B. Wei, Y. Bai, S. Jia, G. Cao, R. Jiang, C. Zhang, E. Gao, X. Chang, J. Li, S. Li, D. Zhu, R. Tai, H. Zhou, J. Wang, M. Zeng, Z. Wang, L. Fu, Ultrathin high-κ antimony oxide single crystals. *Nat. Commun.* **11**, 2502 (2020).
22. C. Tan, H. Zhang, Wet-chemical synthesis and applications of non-layer structured two-dimensional nanomaterials. *Nat. Commun.* **6**, 7873 (2015).
23. W. Tang, W. Fan, W. Zhang, Z. Yang, L. Li, Z. Wang, Y. L. Chiang, Y. Liu, L. Deng, L. He, Z. Shen, O. Jacobson, M. A. Aronova, A. Jin, J. Xie, X. Chen, Wet/sono-chemical synthesis of enzymatic two-dimensional MnO_2 nanosheets for synergistic catalysis-enhanced phototheranostics. *Adv. Mater.* **31**, e1900401 (2019).
24. T. Yang, T. T. Song, M. Callsen, J. Zhou, J. W. Chai, Y. P. Feng, S. J. Wang, M. Yang, Atomically thin 2D transition metal oxides: Structural reconstruction, interaction with substrates, and potential applications. *Adv. Mater. Interfaces* **6**, 1801160 (2018).
25. J. N. Coleman, M. Lotya, A. O'Neill, S. D. Bergin, P. J. King, U. Khan, K. Young, A. Gaucher, S. De, R. J. Smith, I. V. Shvets, S. K. Arora, G. Stanton, H. Y. Kim, K. Lee, G. T. Kim, G. S. Duesberg, T. Hallam, J. J. Boland, J. J. Wang, J. F. Donegan, J. C. Grunlan, G. Moriarty, A. Shmeliov, R. J. Nicholls, J. M. Perkins, E. M. Grieveson, K. Theuwissen, D. W. McComb, P. D. Nellist, V. Nicolosi, Two-dimensional nanosheets produced by liquid exfoliation of layered materials. *Science* **331**, 568–571 (2011).
26. J. M. Lee, B. Kang, Y. K. Jo, S. J. Hwang, Organic intercalant-free liquid exfoliation route to layered metal-oxide nanosheets via the control of electrostatic interlayer interaction. *ACS Appl. Mater. Interfaces* **11**, 12121–12132 (2019).
27. C. Zhang, S.-H. Park, S. E. O'Brien, A. Seral-Ascaso, M. Liang, D. Hanlon, D. Krishnan, A. Crossley, N. McEvoy, J. N. Coleman, V. Nicolosi, Liquid exfoliation of interlayer spacing-tunable 2D vanadium oxide nanosheets: High capacity and rate handling Li-ion battery cathodes. *Nano Energy* **39**, 151–161 (2017).
28. N. Zhou, R. Yang, T. Zhai, Two-dimensional non-layered materials. *Mater. Today Nano* **8**, 100051 (2019).
29. T. S. Khan, M. S. Al-Shehhi, Review of black powder in gas pipelines–An industrial perspective. *J. Nat. Gas Sci. Eng.* **25**, 66–76 (2015).
30. X. Liu, M. Antonietti, Moderating black powder chemistry for the synthesis of doped and highly porous graphene nanoplatelets and their use in electrocatalysis. *Adv. Mater.* **25**, 6284–6290 (2013).
31. S. I. F. S. Martins, W. M. F. Jongen, M. A. J. S. van Boekel, A review of Maillard reaction in food and implications to kinetic modelling. *Trends Food Sci. Technol.* **11**, 364–373 (2000).
32. H. Y. Wang, H. Qian, W.-R. Yao, Melanoidins produced by the Maillard reaction: Structure and biological activity. *Food Chem.* **128**, 573–584 (2011).
33. G. T. Chandrappa, N. Steunou, J. Livage, Materials chemistry: Macroporous crystalline vanadium oxide foam. *Nature* **416**, 702 (2002).
34. M. Pianassola, M. Loveday, J. W. McMurray, M. Koschan, C. L. Melcher, M. Zhuravleva, Solid-state synthesis of multicomponent equiatomic rare-earth oxides. *J. Am. Ceram. Soc.* **103**, 2908–2918 (2020).
35. G. Azimi, R. Dhiman, H. M. Kwon, A. T. Paxson, K. K. Varanasi, Hydrophobicity of rare-earth oxide ceramics. *Nat. Mater.* **12**, 315–320 (2013).
36. S. Sato, R. Takahashi, M. Kobune, H. Gotoh, Basic properties of rare earth oxides. *Appl. Catal. A* **356**, 57–63 (2009).
37. A. Sarkar, Q. Wang, A. Schiele, M. R. Chellali, S. S. Bhattacharya, D. Wang, T. Brezesinski, H. Hahn, L. Velasco, B. Breitung, High-entropy oxides: Fundamental aspects and electrochemical properties. *Adv. Mater.* **31**, e1806236 (2019).

38. A. Sarkar, L. Velasco, D. Wang, Q. Wang, G. Talasil, L. de Biasi, C. Kubel, T. Brezesinski, S. S. Bhattacharya, H. Hahn, B. Breitung, High entropy oxides for reversible energy storage. *Nat. Commun.* **9**, 3400 (2018).

39. H. R. Mao, R. F. Guo, Y. Cao, S.-B. Jin, X.-M. Qiu, P. Shen, Ultrafast densification of high-entropy oxide $(La_{0.2}Nd_{0.2}Sm_{0.2}Eu_{0.2}Gd_{0.2})_2Zr_2O_7$ by reactive flash sintering. *J. Eur. Ceram. Soc.* **41**, 2855–2860 (2021).

40. W. J. Yin, B. Weng, J. Ge, Q. Sun, Z. Li, Y. Yan, Oxide perovskites, double perovskites and derivatives for electrocatalysis, photocatalysis, and photovoltaics. *Energ. Environ. Sci.* **12**, 442–462 (2019).

41. A. Kumar, A. Kumar, V. Krishnan, Perovskite oxide based materials for energy and environment-oriented photocatalysis. *ACS Catal.* **10**, 10253–10315 (2020).

42. X. Wang, Y. Zhang, C. Zhi, X. Wang, D. Tang, Y. Xu, Q. Weng, X. Jiang, M. Mitome, D. Golberg, Y. Bando, Three-dimensional strutted graphene grown by substrate-free sugar blowing for high-power-density supercapacitors. *Nat. Commun.* **4**, 2905 (2013).

43. L. Peng, P. Xiong, L. Ma, Y. Yuan, Y. Zhu, D. Chen, X. Luo, J. Lu, K. Amine, G. Yu, Holey two-dimensional transition metal oxide nanosheets for efficient energy storage. *Nat. Commun.* **8**, 15139 (2017).

44. Q. Guo, X. Li, H. Wei, Y. Liu, L. Li, X. Yang, X. Zhang, H. Liu, Z. Lu Sr., Fe Co-doped perovskite oxides with high performance for oxygen evolution reaction. *Front. Chem.* **7**, 224 (2019).

45. Q. A. Islam, R. Majee, S. Bhattacharyya, Bimetallic nanoparticle decorated perovskite oxide for state-of-the-art trifunctional electrocatalysis. *J. Mater. Chem. A* **7**, 19453–19464 (2019).

46. R. Zong, Y. Fang, C. Zhu, X. Zhang, L. Wu, X. Hou, Y. Tao, J. Shao, Surface defect engineering on perovskite oxides as efficient bifunctional electrocatalysts for water splitting. *ACS Appl. Mater. Interfaces* **13**, 42852–42860 (2021).

47. D. Ji, C. Liu, Y. Yao, L. Luo, W. Wang, Z. Chen, Cerium substitution in $LaCoO_3$ perovskite oxide as bifunctional electrocatalysts for hydrogen and oxygen evolution reactions. *Nanoscale* **13**, 9952–9959 (2021).

48. Y. Yi, Q. Wu, J. Li, W. Yao, C. Cui, Phase-segregated $SrCo_{0.8}Fe_{0.5-x}O_{3-\delta}/Fe_xO_y$ heterostructured catalyst promotes alkaline oxygen evolution reaction. *ACS Appl. Mater. Interfaces* **13**, 17439–17449 (2021).

49. Z. Li, K. H. Xue, J. Wang, J. G. Li, X. Ao, H. Sun, X. Song, W. Lei, Y. Cao, C. Wang, Cation and anion co-doped perovskite nanofibers for highly efficient electrocatalytic oxygen evolution. *ACS Appl. Mater. Interfaces* **12**, 41259–41268 (2020).

50. Y. Zhu, W. Zhou, J. Yu, Y. Chen, M. Liu, Z. Shao, Enhancing electrocatalytic activity of perovskite oxides by tuning cation deficiency for oxygen reduction and evolution reactions. *Chem. Mater.* **28**, 1691–1697 (2016).

51. Y. Zhu, W. Zhou, Y. Zhong, Y. Bu, X. Chen, Q. Zhong, M. Liu, Z. Shao, A perovskite nanorod as bifunctional electrocatalyst for overall water splitting. *Adv. Energy Mater.* **7**, (2017).

52. Y. Bu, O. Gwon, G. Nam, H. Jang, S. Kim, Q. Zhong, J. Cho, G. Kim, A highly efficient and robust cation ordered perovskite oxide as a bifunctional catalyst for rechargeable zinc-air batteries. *ACS Nano* **11**, 11594–11601 (2017).

53. Y. Zhu, Q. Lin, Z. Hu, Y. Chen, Y. Yin, H. A. Tahini, H. J. Lin, C. T. Chen, X. Zhang, Z. Shao, H. Wang, Self-assembled ruddlesden-popper/perovskite hybrid with lattice-oxygen activation as a superior oxygen evolution electrocatalyst. *Small* **16**, e2001204 (2020).

54. S. She, J. Yu, W. Tang, Y. Zhu, Y. Chen, J. Sunarso, W. Zhou, Z. Shao, Systematic study of oxygen evolution activity and stability on $La_{1-x}Sr_xFeO_{3-\delta}$ perovskite electrocatalysts in alkaline media. *ACS Appl. Mater. Interfaces* **10**, 11715–11721 (2018).

55. Y. Zhu, W. Zhou, Z. G. Chen, Y. Chen, C. Su, M. O. Tade, Z. Shao, $SrNb_{0.1}Co_{0.7}Fe_{0.2}O_{3-\delta}$ perovskite as a next-generation electrocatalyst for oxygen evolution in alkaline solution. *Angew. Chem. Int. Ed.* **54**, 3897–3901 (2015).

56. N. I. Kim, Y. J. Sa, T. S. Yoo, S. R. Choi, R. A. Afzal, T. Choi, Y. S. Seo, K. S. Lee, J. Y. Hwang, W. S. Choi, S. H. Joo, J. Y. Park, Oxygen-deficient triple perovskites as highly active and durable bifunctional electrocatalysts for oxygen electrode reactions. *Sci. Adv.* **4**, eaap9360 (2018).